PHOTONICS Research

Fully integrated and broadband Si-rich silicon nitride wavelength converter based on Bragg scattering intermodal four-wave mixing

Valerio Vitali,[1,2,*] Thalía Domínguez Bucio,[1] Hao Liu,[1] José Manuel Luque González,[3] Francisco Jurado-Romero,[3] Alejandro Ortega-Moñux,[3] Glenn Churchill,[1] James C. Gates,[1] James Hillier,[4,5] Nikolaos Kalfagiannis,[4,6] Daniele Melati,[7] Jens H. Schmid,[8] Ilaria Cristiani,[2] Pavel Cheben,[8] J. Gonzalo Wangüemert-Pérez,[3] Íñigo Molina-Fernández,[3] Frederic Gardes,[1] Cosimo Lacava,[2] and Periklis Petropoulos[1]

[1]Optoelectronics Research Centre, University of Southampton, Southampton SO17 1BJ, UK
[2]Electrical, Computer and Biomedical Engineering Department, University of Pavia, Pavia 27100, Italy
[3]Telecommunication Research Institute (TELMA), Universidad de Málaga, CEI Andalucía TECH, E.T.S.I. Telecomunicación, 29010 Málaga, Spain
[4]School of Science and Technology, Nottingham Trent University, Nottingham NG11 8NS, UK
[5]Department of Electrical Engineering, Eindhoven University of Technology, Eindhoven 5600 MB, The Netherlands
[6]Department of Materials Science and Engineering, University of Ioannina, Ioannina 45110, Greece
[7]Centre de Nanosciences et de Nanotechnologies, Université Paris-Saclay, CNRS, 91120 Palaiseau, France
[8]Advanced Electronics and Photonics Research Center, National Research Council Canada, Ottawa, Ontario K1A 0R6, Canada
*Corresponding author: valerio.vitali@unipv.it

Received 22 September 2023; revised 12 November 2023; accepted 13 November 2023; posted 21 November 2023 (Doc. ID 506691); published 29 February 2024

Intermodal four-wave mixing (FWM) processes have recently attracted significant interest for all-optical signal processing applications thanks to the possibility to control the propagation properties of waves exciting distinct spatial modes of the same waveguide. This allows, in principle, to place signals in different spectral regions and satisfy the phase matching condition over considerably larger bandwidths compared to intramodal processes. However, the demonstrations reported so far have shown a limited bandwidth and suffered from the lack of on-chip components designed for broadband manipulation of different modes. We demonstrate here a silicon-rich silicon nitride wavelength converter based on Bragg scattering intermodal FWM, which integrates mode conversion, multiplexing and de-multiplexing functionalities on-chip. The system enables wavelength conversion between pump waves and a signal located in different telecommunication bands (separated by 60 nm) with a 3 dB bandwidth exceeding 70 nm, which represents, to our knowledge, the widest bandwidth ever achieved in an intermodal FWM-based system.

https://doi.org/10.1364/PRJ.506691

1. INTRODUCTION

Present optical transmission systems need to cope with an ever-growing demand for bandwidth to transmit the continuously growing amount of data generated across the world. A paradigm shift in optical networks and photonic devices will be required to tackle this challenge and increase the efficiency of the current wavelength division multiplexing (WDM)-based optical communication systems [1]. While techniques based on space division multiplexing hold significant promise [2–4], a complementary attractive route to increasing the capacity of optical networks comes from the observation that current systems make use of only a small portion of the wide low-loss bandwidth of silica optical fibers. In this regard, configurations that exploit optical wavelength bands outside the conventional C-band spectrum (1530–1565 nm) are currently being investigated [5,6]. One particularly attractive option is represented by the use of the adjacent L- (1565–1625 nm) and U-bands (1625–1675 nm). Similar to the C-band, in these new systems, the ability to generate, convert and manipulate optical signals is highly desirable. Third-order-nonlinearity-based optical devices could be used to generate and convert wavelength components through well-studied parametric optical processes such as those based on four-wave mixing (FWM) [7]. Various demonstrations have already been reported for the realization of wavelength converters and synthesizers capable of operating over a broad wavelength range, mainly based on the use of integrated

waveguides [8–10]. In general, most of these demonstrations have exploited nonlinear processes based on intramodal FWM, i.e., where all the waves propagate in the same optical spatial mode. More recently, integrated systems based on intermodal FWM (IM-FWM) processes, i.e., where the involved waves propagate in different spatial modes of the same waveguide, have been studied, and have shown considerable potential to respond to the requirements of next-generation communication systems. Indeed, the introduction of additional modes in nonlinear waveguides offers an extra degree of freedom in dispersion engineering to fulfil the required phase matching condition thanks to the possibility of tuning the characteristics of distinct spatial modes over the wavelengths of interest. This allows in principle for broadband operation in multiple spectral bands of the electromagnetic spectrum, even located hundreds of nanometers away from the pump source(s) [11,12]. Several demonstrations of IM-based applications have already been shown, such as supercontinuum generation [13–15], comb generation [16,17], signal processing based on stimulated IM Brillouin scattering [18,19], wavelength conversion [12,20–24] and the realization of photon pair sources for quantum applications [25–27]. Most of these demonstrations made use of either degenerate or non-degenerate parametric amplification, where the idler generation is accompanied by the amplification of vacuum fluctuations, which inherently adds excess noise to the process [28,29]. However, in both the classical and quantum regimes, minimum excess noise is desirable since additional noise can result in higher bit-error rates in classical telecommunication systems and poor fidelity of translated quantum states in quantum systems [30,31]. An alternative non-degenerate FWM process, termed Bragg scattering (BS) FWM, does not amplify vacuum fluctuations and, therefore, can in principle convert photons from the signal to the idler frequency without excess noise [30,32]. Some promising wavelength converters implementing a BS-IM-FWM configuration have already been reported in the C- and L-bands using integrated waveguides [20,21]. These first demonstrations showed the potential of the BS-IM-FWM process; however, their experimental implementations were complex and suffered from the lack of integrated components for manipulating the spatial shapes of the involved optical modes on-chip, eventually adding further losses to the whole system. As a consequence, this limited the conversion efficiency of the proposed devices, even when relatively high pump power levels were employed, and, ultimately, the achievable bandwidth due to the use of bulky off-chip components to manipulate the involved optical modes.

In this paper, we present the design and experimental characterization of a fully integrated and broadband wavelength converter based on the use of the BS-IM-FWM process implemented on a silicon-rich silicon nitride (Si-rich SiN) platform. The system integrates the whole set of functionalities required to perform frequency conversion on-chip in the IM regime, starting from three seeding waves (two pumps and one signal), which are coupled from an array of lensed single-mode optical fibers. This eliminates the requirement for external and bulky mode conversion, multiplexing and demultiplexing elements, significantly reduces the insertion losses of the whole system and eliminates the need of filtering out the optical pumps at the device output. The proposed device is capable of generating idler wavelengths covering the range of 1600–1678 nm starting from a seeding signal at 1600 nm, with an experimentally measured 3 dB bandwidth greater than 70 nm, by utilizing optical pumps located in the wavelength range of 1540–1616 nm. To the best of the authors' knowledge, this represents the widest bandwidth ever achieved in a multimode FWM-based device.

2. BRAGG SCATTERING INTERMODAL FWM SCHEME

A general illustration of the BS-FWM process is shown in Fig. 1(a). As can be seen, BS-FWM enables the generation of blue and red shifted copies ($I_{BS,b}$ and $I_{BS,r}$ idlers, respectively) of the seeding signal (S) through a scattering process induced by an intensity grating caused by the interference between the two pumps (P_1 and P_2). The values of the idler frequencies are determined by the energy conservation law, i.e., they appear at $\omega_S \pm \Delta\omega$, where ω_S stands for the signal frequency and $\Delta\omega$ is the frequency difference between the two pumps. As in any FWM-based process, efficient conversion is ensured only when the interacting waves satisfy the phase matching condition. This can generally be achieved only for one idler at a time, and, in most cases, the other non-phase-matched idler

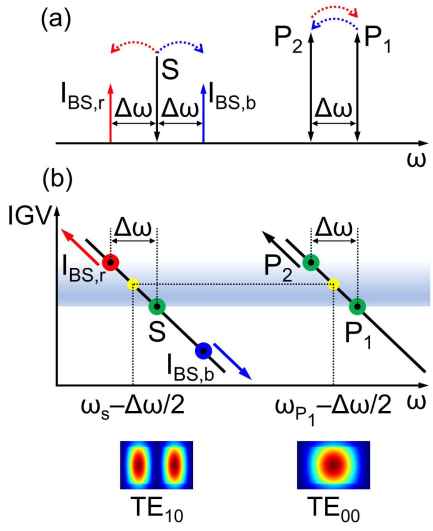

Fig. 1. (a) Dual-pump BS FWM working principle. When two pumps (P_1 and P_2) and a seeding signal (S) are input into a third-order nonlinear waveguide, BS FWM can occur under the assumption that the phase matching condition is fulfilled. In this scenario, photons are scattered from the signal S to two idlers ($I_{BS,b}$ and $I_{BS,r}$), with a simultaneous energy exchange between the two pumps. The solid arrows indicate the loss (down) and gain (up) of the photon energy, while the dashed arrows indicate the direction of the energy exchange for the $I_{BS,r}$ (red) and $I_{BS,b}$ (blue) cases. (b) Graphical illustration of the phase matching mechanism for the BS-IM-FWM scheme. If P_1 and P_2 are placed in the TE_{00} mode and the signal and idlers in the TE_{10} mode of a multimode waveguide, the phase matching condition can be satisfied and retained if it is possible to draw a horizontal line that crosses the IGV curves of the two considered modes at the average frequencies (yellow dots in the figure) of the two pumps and of the signal and one idler (either $I_{BS,b}$ or $I_{BS,r}$).

represents an unwanted by-product of the nonlinear process. In the case of single-mode waveguides, phase matching is commonly accomplished by carefully designing the waveguide geometry to engineer the group velocity dispersion [33]. Specifically, in order to achieve efficient BS FWM, the waveguide needs to exhibit zero dispersion at the half-distance between the average frequency of the signal–idler pair and that of the pair of pumps [30,34]. However, in the IM regime, the phase matching condition gives rise to different requirements. An illustrative schematic of the operating principle to satisfy the phase matching condition in the BS-IM-FWM configuration is illustrated in Fig. 1(b) [20,35,36], which shows the inverse group velocity (IGV) curves of two distinct spatial modes supported in a multimode waveguide as a function of the angular frequency ω. The inverse group velocity is defined as $\mathrm{IGV} = v_g^{-1} = n_g/c$, where v_g is the group velocity, n_g is the group index and c is the speed of light in vacuum.

In our simulations and experiments, P_1 and P_2 were placed into the fundamental TE-polarized waveguide mode (TE_{00}), while the signal S and the generated idlers $I_{BS,b}$ and $I_{BS,r}$ were in the first-order TE-polarized horizontal mode (TE_{10}). Considering the $I_{BS,r}$ idler, phase matching is ensured when the following equation is fulfilled [20]:

$$-\beta^0(\omega_{P1}) + \beta^1(\omega_S) + \beta^0(\omega_{P2}) - \beta^1(\omega_{BS,r}) = 0, \quad \textbf{(1)}$$

where $\beta^0(\omega)$ and $\beta^1(\omega)$ are the propagation constants of the TE_{00} and TE_{10} modes at the angular frequency ω, respectively, and ω_{P1}, ω_{P2}, ω_S and $\omega_{BS,r}$ stand for the angular frequencies of pump 1, pump 2, signal and red shifted BS idler, respectively. Equation (1) can be rewritten as

$$\beta^0(\omega_{P1}) - \beta^0(\omega_{P1} - \Delta\omega) = \beta^1(\omega_S) - \beta^1(\omega_s - \Delta\omega). \quad \textbf{(2)}$$

Under the assumption of a small frequency detuning ($\Delta\omega \approx 0$), Eq. (2) shows that phase matching is satisfied when the derivative function of the propagation constant in one mode (β^0), which is its IGV, evaluated at the P_1 frequency ω_{P1}, is equal to the derivative function of the propagation constant in the other mode (β^1), calculated at the signal frequency ω_S. Therefore, any possible frequency combinations to achieve phase matching across the two modes (or various modes, in case higher-order modes are also considered) can be found by the crossing of any horizontal line drawn on the IGV curves of Fig. 1(b). For a greater $\Delta\omega$ detuning, if P_2 is tuned towards shorter frequencies, $\omega_{BS,r}$ moves in the same direction, and it is still possible to draw an upshifted horizontal line crossing the two IGV curves at the new average frequencies ($\omega_{P1} - \Delta\omega/2$ and $\omega_S - \Delta\omega/2$), provided that each IGV curve is a frequency-shifted replica of the other. Conversely, the $I_{BS,b}$ idler component, even though it satisfies the energy conservation principle as $I_{BS,r}$, is shown to not satisfy the phase matching condition in the reported example because it is only possible to draw an oblique line to cross the two IGV points at the new average frequencies. As the P_2 detuning to lower frequencies increases, $I_{BS,b}$ moves further away from phase matching. It should be noted that if the P_1 frequency is tuned to higher ω values, the opposite scenario holds true: a broadband operation can be achieved for $I_{BS,b}$, whereas $I_{BS,r}$ quickly moves away from phase matching as $\Delta\omega$ increases. The presented phase matching mechanism can be exploited to efficiently suppress one idler component to achieve a unidirectional FWM process, as already demonstrated in Ref. [20]. Interestingly, this scheme can be applied to any pair of supported waveguide modes. When a higher-order mode is considered, the frequency separation between the pumps and the signal–idlers can be further increased. Therefore, provided that the IGV curves of the considered modes meet the criteria described above, the phase matching condition can still be satisfied even for extremely large pump-to-signal frequency detuning values. The described properties of the BS-IM-FWM differ significantly from the ones of the single-mode case and pose less stringent requirements on the engineering of the dispersion and dispersion slope profiles of the waveguide, thus providing more flexibility on the design of wavelength converters, especially when a large wavelength detuning is desirable.

3. NONLINEAR MULTIMODE WAVEGUIDE DESIGN

The nonlinear multimode waveguide was designed for our in-house Si-rich SiN platform, consisting of a Si-rich SiN strip waveguide surrounded by a silicon dioxide (SiO_2) cladding. This material platform allows excellent dispersion engineering control and precise tuning of the propagation characteristics of the supported modes by varying the waveguide geometry and the refractive index of the core material itself, which can be controlled by changing the Si-rich SiN deposition conditions [37]. In addition, the material can be engineered to show a high Kerr coefficient with no two-photon absorption (TPA)-related losses in the telecommunication bands [38]. Figure 2 shows the cross-section of the designed waveguide (6.1 μm width × 310 nm height) and the simulated group index n_g curves as a function of wavelength λ for the first two considered modes (TE_{00} and TE_{10}). The refractive index of the Si-rich SiN core material (Si_xN_y) was set equal to 2.41 at 1550 nm by adjusting the silicon content within the silicon nitride host matrix in the deposition process [37]. The waveguide cross-section was engineered to achieve the phase matching condition between the TE_{00} and TE_{10} modes at wavelengths $\lambda_{TE00} = 1540$ nm and $\lambda_{TE10} = 1600$ nm, respectively. In our experiments, the two pumps P_1 and P_2 were placed in the TE_{00} mode, while the

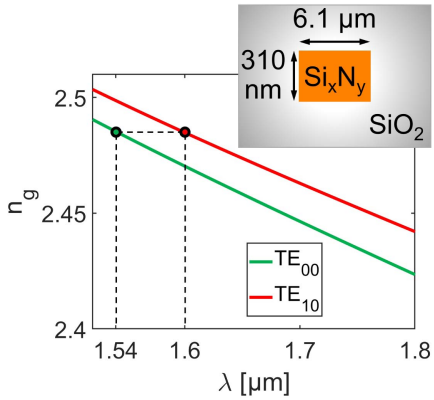

Fig. 2. Numerically simulated group index n_g for the first two horizontal modes TE_{00} and TE_{10} as a function of wavelength λ and sketch of the cross-section of the Si-rich SiN multimode waveguide employed in this work (note that dimensions are not to scale).

signal S and the generated idlers were in the TE_{10} mode. As can be seen from Fig. 2, the nonlinear multimode waveguide was designed so that the two n_g curves, which are proportional to the IGV curves, are a frequency-shifted replica of each other to ensure a wide conversion bandwidth.

By considering this specific mode and wavelength configuration, the bandwidth of the BS-IM-FWM process in terms of conversion efficiency (CE) for both $I_{BS,b}$ and $I_{BS,r}$ was numerically calculated as a function of the pump and signal wavelength detuning. The CE was defined as $CE = P_I(L_{MM})/P_S(L_{MM})$, where $P_I(L_{MM})$ is the optical power of the $I_{BS,b}$ or $I_{BS,r}$ idler and $P_S(L_{MM})$ is the signal S power evaluated at the output of the nonlinear multimode waveguide (with length L_{MM}), respectively. The two waveguide modes and their dispersion profiles were numerically calculated using a Finite Difference Eigenmode (FDE) solver from MODE Solutions (Ansys Inc.). For the Si-rich SiN core, the refractive index profile was experimentally acquired via infrared (IR) spectroscopic ellipsometry measurements performed on the bulk material employed in this work, while the data reported by Palik were used for the SiO_2 cladding [39]. The numerically simulated modal effective index profiles and mode overlap factors were used for nonlinear wave propagation simulations based on the fourth-order Runge–Kutta method [40]. Further details about the coupled equations used to model the BS-IM-FWM process can be found in Ref. [21]. The nonlinear Kerr coefficient was set to $n_2 = 1.56 \times 10^{-18}$ m^2/W, which was experimentally measured as described in Ref. [37], while the nonlinear waveguide length was set equal to $L_{MM} = 1$ cm. A propagation loss coefficient $\alpha = 2.3$ dB/cm was considered. In these simulations, the wavelength of P_1 was kept fixed at 1540 nm, while the wavelengths of P_2 and signal S were varied. In all cases, the total pump power level was kept at 27.6 dBm (24.6 dBm per pump), while the signal power was set at 8 dBm, as in the nonlinear experiments. Figure 3 reports the normalized CE results from the numerical simulations for the $I_{BS,b}$ and $I_{BS,r}$ in Figs. 3(a) and 3(b), respectively. By considering a signal-detuning close to zero (corresponding to the signal set close to the nominal designed wavelength $\lambda_S = 1600$ nm), an (almost) constant CE level can be obtained for $I_{BS,r}$ even for extremely large P_2 detuning values (>80 nm). On the other hand, $I_{BS,b}$ is hindered in this scenario, and phase matching is only achieved over a significantly narrower P_2 detuning range compared to the $I_{BS,r}$ case. In addition, Fig. 3(b) also shows that even for P_2 detuning values as large as 30 nm, the conversion process to $I_{BS,r}$ is (almost) insensitive to the signal wavelength for a signal-detuning bandwidth of ≈18 nm around $\lambda_S = 1600$ nm, with no significant degradation in CE (<1 dB variation).

The fabrication tolerance of the nonlinear multimode waveguide was then evaluated to estimate the impact of dimension variations on the position of the phase-matched signal wavelength relative to the nominal design value of 1600 nm. By considering a ±30 nm variation of the waveguide width and thickness, shifts of approximately ∓1 nm and ±9 nm in the position of the phase-matched signal wavelength were found, respectively, showing good fabrication tolerance. As discussed in the previous section, the use of higher-order modes would allow, in principle, to achieve an even larger separation between the pumps and signal–idler pairs. For example, considering the multimode waveguide cross-section used in this work (6.1 μm width × 310 nm height), by setting the two pumps in the TE_{00} mode with P_1 fixed at 1540 nm, the phase-matched signal wavelengths would move to ≈1730 nm and ≈2110 nm when the TE_{20} and TE_{30} modes are employed for the signal–idler pairs, respectively. The use of higher-order modes would require a modification of the design of the different components for mode conversion and manipulation at longer wavelengths, which may be of interest for future studies targeting mid-infrared (MIR) frequency generation.

4. DEVICE LAYOUT AND WORKING PRINCIPLE

A schematic layout of the full device and its working principle is shown in Fig. 4. The system consists of five different blocks: input section, mode converter and multiplexer (mode-MUX), nonlinear multimode waveguide, mode converter and demultiplexer (mode-DEMUX) and output section. In the input section, inverted-taper-based edge couplers (ECs) were designed to efficiently couple signals incoming from lensed single-mode polarization-maintaining (PM) optical fibers. A two-fiber array (FA) was used to simultaneously couple the two pumps (P_1 and P_2) into port 1 of the device and the signal (S) into port 2.

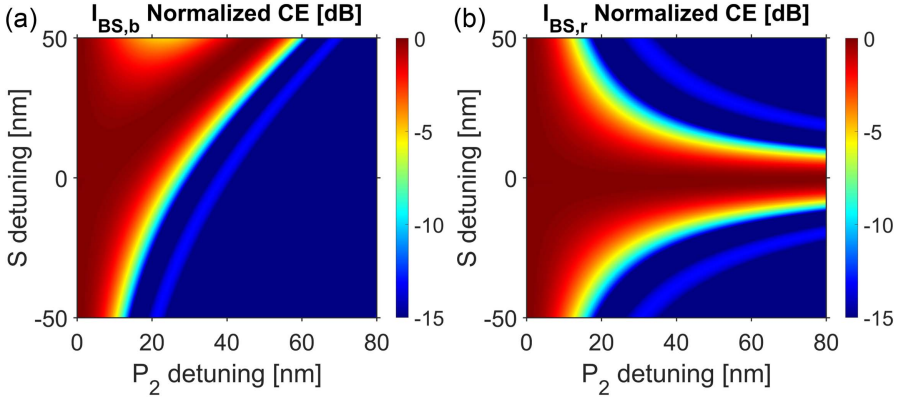

Fig. 3. Simulated BS-IM-FWM normalized CE for different P_2 and S detuning values for (a) $I_{BS,b}$ and (b) $I_{BS,r}$. The P_1 wavelength was set equal to $\lambda_{P1} = 1540$ nm for all the considered cases. The phase matching wavelength for the signal S is $\lambda_S = 1600$ nm (which corresponds to a signal-detuning equal to zero).

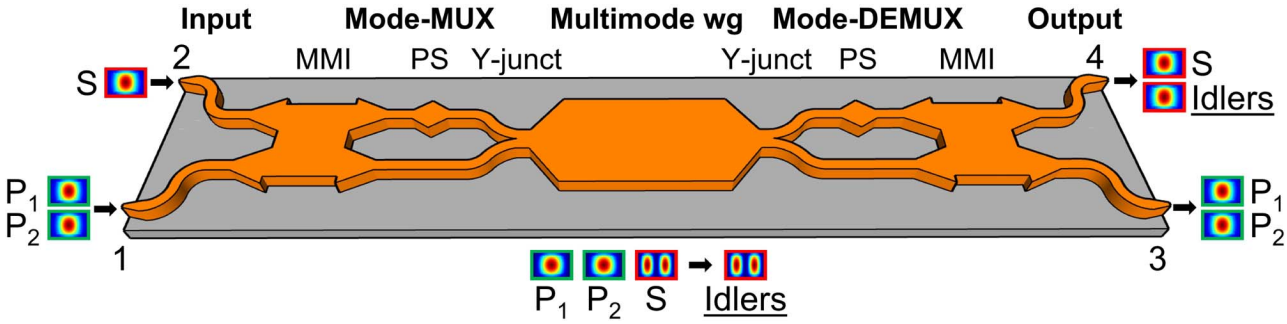

Fig. 4. Schematic layout and working principle of the fully integrated intermodal FWM-based wavelength converter. P_1, pump 1; P_2, pump 2; S, signal; MMI, multimode interference coupler; PS, phase shifter; Y-junct, Y-junction; mode-MUX, mode converter and multiplexer; wg, waveguide; mode-DEMUX, mode converter and demultiplexer.

The ECs were connected to the mode-MUX through bent single-mode waveguides. The mode-MUX comprised a multimode interference (MMI) coupler, a 90° phase shifter (PS) and a sinusoidal-profile symmetric Y-junction (overall footprint of the mode-MUX: 4 μm × 121 μm). The mode-MUX was designed according to the following working principle [41,42]: a TE_{00} mode input from port 1 was equally split by the MMI and a +90° phase shift was induced between the modes propagating through the MMI upper and lower output arms. Afterwards, the PS introduced a −90° phase shift between the mode propagating through the upper arm and the mode propagating through the lower arm, eliminating the phase difference between the two optical modes. Hence, two in-phase TE_{00} modes reached the symmetric Y-junction and underwent conversion into the fundamental TE_{00} mode of the multimode waveguide. Conversely, a TE_{00} mode coupled into port 2 was also equally split by the MMI, but, in this case, a −90° phase shift was induced between the modes propagating through the MMI upper and lower output arms. Therefore, after propagating through the PS section, two out-of-phase (180° overall phase shift) TE_{00} modes reached the symmetric Y-junction and underwent conversion to the TE_{10} mode of the multimode waveguide. In this manner, the two pumps coupled in from port 1 excited the TE_{00} mode of the multimode waveguide, while the signal coupled in from port 2 excited the TE_{10} mode. The BS-IM-FWM process then occurred in the multimode waveguide (length $L_{MM} = 1$ cm, whole device length = 1.14 cm) with the generation of $I_{BS,b}$ and $I_{BS,r}$ idlers in the TE_{10} mode. Next, a mode-DEMUX and output section performed the reciprocal operation of the input section and mode-MUX. The two residual pump waves were maintained in the TE_{00} mode and coupled out from port 3, while the signal and idler waves in the TE_{10} mode were converted to the TE_{00} mode by the mode-DEMUX and coupled out from port 4. As at the side of the input, a two-fiber array was used to simultaneously couple out all the waves from the two output ports. It is worth noticing that this configuration allowed separating the signal and idler waves from the two optical pumps, therefore eliminating by design the requirement to filter the high-power pumps out from the desired signals. The geometrical dimensions of the designed device are listed in Appendix A.

5. FABRICATION

The proposed device was fabricated on a 200 mm Si wafer with a 3 μm thermally grown oxide layer as a starting substrate. The 310 nm thick Si-rich SiN device layer, with a refractive index of 2.41 at 1550 nm, was deposited at a low processing temperature (350°C) using a NH_3-free plasma enhanced chemical vapor deposition (PECVD) process, as detailed in Refs. [37,43]. Afterwards, the test structures were patterned with a 248 nm deep-UV (DUV) lithography tool using a 680 nm thick positive tone resist mask with a 60 nm thick bottom anti-reflection coating (BARC). The BARC layer was included to reduce the sidewall roughness generated by the back-reflected light during the lithography process, which can have a detrimental effect on the propagation losses of the fabricated devices. The pattern was then transferred onto the Si-rich SiN layer by means of an inductively coupled plasma (ICP) etching process using a SF_6:C_4F_8 chemistry with an

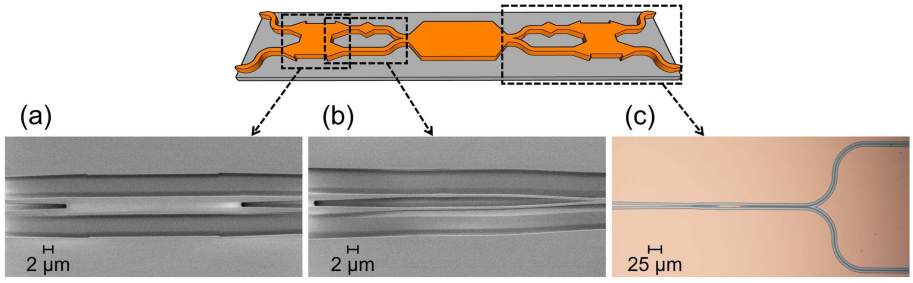

Fig. 5. Schematic layout of the fabricated device along with top-view SEM images of (a) MMI, (b) PS and Y-junction sections of the mode-MUX and (c) an optical microscope image of the full mode-DEMUX and output section.

etching depth of 310 nm. The resist mask was then removed using an O_2 plasma process and an RCA-1 cleaning step. Finally, a 2 μm thick PECVD SiO_2 layer was deposited as cladding. Figure 5 shows a schematic diagram of the device along with scanning electron microscope (SEM) images of the top-view of the MMI [Fig. 5(a)], PS and Y-junction [Fig. 5(b)] sections of the device and an optical microscope image of the full mode-DEMUX and output section [Fig. 5(c)].

The input and output facets were prepared by dicing, a type of mechanical sawing that uses diamond grit-impregnated blades, traditionally employed to separate individual dies from a wafer. Through careful selection of blade composition and cutting parameters, ductile removal of optical materials can be achieved, resulting in sub-nanometer roughness [44]. High-quality facets with negligible chipping and delamination of material layers were produced in a single step with no requirement for time-consuming polishing [45]. The coupling losses per facet between a lensed single-mode PM optical fiber (spot diameter of 3.5 μm) and the inverted-taper-based EC were assessed to be 1.4 dB, while the propagation losses of the nonlinear multimode waveguide were measured to be equal to 2.3 dB/cm at 1550 nm.

6. EXPERIMENTAL RESULTS

The linear performance of the full device was initially evaluated. Figure 6 shows the measured fiber-to-fiber transmission curves between the two input ports (1, 2) and output ports (3, 4). Considering the transmission curves between ports 1 to 3 (input: TE_{00}, multimode waveguide: TE_{00}, output: TE_{00}) and ports 2 to 4 (input: TE_{00}, multimode waveguide: TE_{10}, output: TE_{00}), a minimum fiber-to-fiber loss of ≈5 dB was measured around 1580 nm, with a maximum variation lower than 2 dB in the measured wavelength range 1535–1650 nm. The unwanted transmission between crossing input–output ports (ports 1 to 4 and ports 2 to 3) was also measured, resulting in a minimum loss value of 17 dB. Overall, the device shows a crosstalk value lower than −10 dB between direct and crossing port-to-port transmissions in the measured wavelength range. Considering the individual components, the full device bandwidth and crosstalk performance are ultimately limited by the spectral response of the tapered 90° PS, which also represents the most sensitive element to fabrication imperfections. In order to reduce the device crosstalk and expand the operational bandwidth, the use of subwavelength grating PSs could be considered. These structures have also shown greater robustness to fabrication errors compared to conventional devices, as already demonstrated in previous works [46,47].

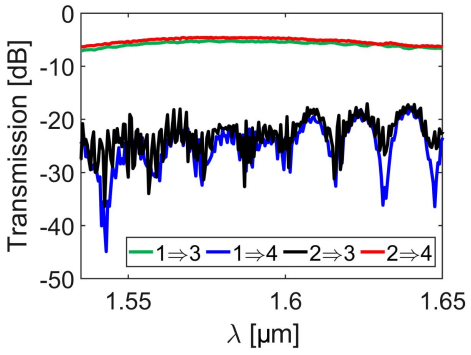

Fig. 6. Linear characterization of the full device: measured transmission curves as a function of wavelength for the different combinations of input–output ports.

Nonlinear measurements were then carried out using the setup shown in Fig. 7. The continuous wave (CW) optical pumps (P_1 and P_2) were generated using two PM tunable laser sources (TLSs) followed by two PM erbium-doped fiber amplifiers (EDFAs). The pumps, after passing through two optical isolators, were coupled together with a 50:50 PM fiber coupler and sent to port 1 of the integrated device. The signal (S) was generated using a third PM TLS and directly sent to port 2 of the integrated device. At the device output, the two residual pumps on port 3 along with the signal and idlers on port 4 were collected and sent to an optical spectrum analyzer (OSA) using an optical switch. One input and one output FA with two lensed PM optical fibers each were used to couple the signals in and out of the device.

Two different sets of nonlinear experiments were performed using a total pump power of 27.6 dBm (24.6 dBm per pump) and a signal power of 8 dBm coupled into the chip. In the first set of measurements, the first pump P_1 was set at 1540 nm (as in the numerical simulations), while the wavelength of the second pump P_2 was scanned from 1542 to 1616 nm in order to characterize the pump-to-pump detuning bandwidth of the BS-IM-FWM process for both the $I_{BS,b}$ and $I_{BS,r}$ idlers. According to the previously presented numerical simulations, the signal S was placed at 1600 nm in order to ensure phase matching with P_1. Figure 8(a) reports the CE measured for the $I_{BS,b}$ (blue squares) and $I_{BS,r}$ (red diamonds) idlers as a function of the pump-to-pump detuning $\Delta\lambda_{PP}$.

A small CE decrease for increasing $\Delta\lambda_{PP}$ can be observed for $I_{BS,r}$, with a 3 dB pump-to-pump detuning bandwidth of

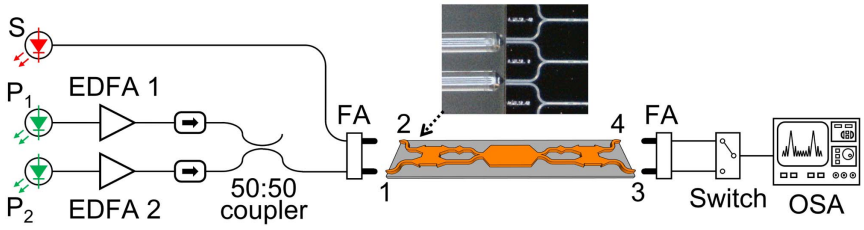

Fig. 7. Sketch of the experimental setup used in the nonlinear experiments. P_1, pump 1; P_2, pump 2; S, signal; EDFA, erbium-doped fiber amplifier; FA, fiber array; OSA, optical spectrum analyzer. The inset shows a microscope image of the optical coupling between the input FA and the on-chip integrated device.

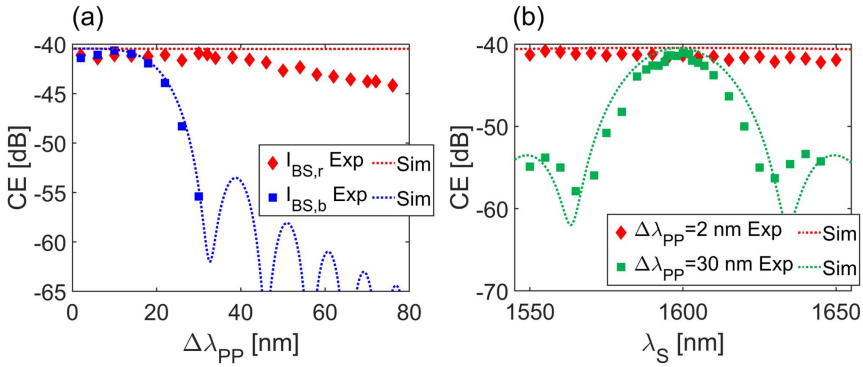

Fig. 8. (a) Experimentally measured CE for the $I_{BS,r}$ (red diamonds) and $I_{BS,b}$ (blue squares) idlers and corresponding numerically simulated CE (red and blue dashed lines, respectively) as a function of the P_2 detuning with P_1 and S wavelengths fixed at 1540 and 1600 nm, respectively. (b) Experimentally measured CE for the $I_{BS,r}$ idler as a function of the signal wavelength λ_S for a P_2 detuning of 2 nm (red diamonds, pump-to-pump detuning $\Delta\lambda_{PP} = 2$ nm) and 30 nm (green squares, $\Delta\lambda_{PP} = 30$ nm) and corresponding numerically simulated CE (red and green dashed lines, respectively), with P_1 wavelength fixed at 1540 nm.

72 nm, corresponding to an idler generated in the range of 1602–1678 nm. Conversely, as expected, a much narrower 3 dB pump-to-pump detuning bandwidth of ≈20 nm was measured for $I_{BS,b}$. Numerical simulations were carried out by considering the pump power values used in the experiments and the measured propagation losses of the multimode waveguide, with the results reported in Fig. 8(a) (blue and red dashed lines for $I_{BS,b}$ and $I_{BS,r}$, respectively) showing a good agreement with the experimental results. The decrease in the experimentally measured $I_{BS,r}$ CE observed for the greater $\Delta\lambda_{PP}$ detuning values can be mainly attributed to the linear transfer function of the full device (see ports 2 to 4 curve in Fig. 6, which shows a decreasing transmission for longer wavelengths in the L- and U-bands). Three examples of optical spectra measured at port 4 are reported in Figs. 9(a)–9(c) for P_2 detuning values of 2, 26 and 76 nm, respectively. As can be seen, an almost constant power level for $I_{BS,r}$ was recorded for the three different P_2 detuning values. Despite the total pump power being significantly (≈20 dB) higher than the signal power at the chip input, the power level measured at port 4 for the two pumps, P_1 and P_2, is comparable to that of the signal S, since most of the power of the two pumps is sent to port 3. It is also noteworthy that, for small P_2 detuning values [e.g. Figs. 9(a) and 9(b)], intra-modal FWM components are also generated (i_1 and i_2), which result from the degenerate FWM process between the two pumps (both of them placed in the TE_{00} mode).

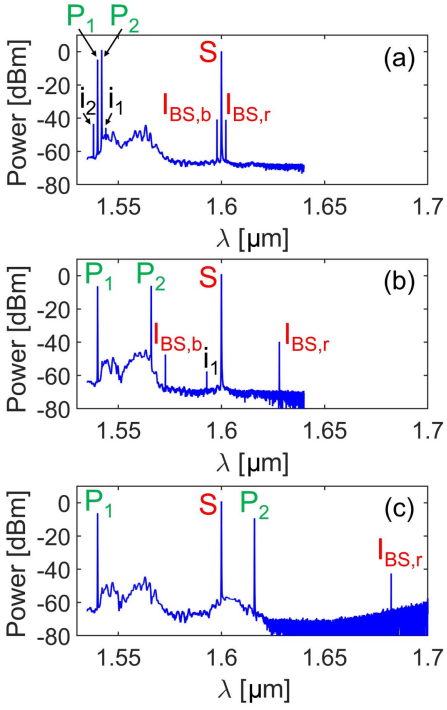

Fig. 9. Optical spectra measured at port 4 for P_2 detuning values $\Delta\lambda_{PP}$ of (a) 2 nm, (b) 26 nm and (c) 76 nm. The wavelengths of P_1 and S are set at 1540 and 1600 nm, respectively.

In the second measurement campaign, the signal-detuning bandwidth was evaluated: P_1 and P_2 were initially placed at 1540 and 1542 nm ($\Delta\lambda_{PP} = 2$ nm), respectively, while the signal wavelength was varied between 1550 and 1650 nm. Using this wavelength setting, the CE values for the $I_{BS,r}$ idler were measured. The results are reported in Fig. 8(b) (red diamonds) and show no significant CE decrease, even for a large signal-detuning of ±50 nm relative to the predicted central signal wavelength of 1600 nm. The experiments were then repeated placing P_1 and P_2 at 1540 and 1570 nm ($\Delta\lambda_{PP} = 30$ nm), respectively, and the resulting CE values for the $I_{BS,r}$ idler are reported in Fig. 8(b) (green squares). In this configuration, the phase matching was not retained across the entire range of scanned signal wavelengths, and a 3 dB signal-detuning bandwidth of ≈25 nm was measured, centered at around 1600 nm. Even in this case, the experimental results are in good agreement with numerical simulations [see Fig. 8(b), red and green dashed lines for pump-to-pump detuning values of 2 and 30 nm, respectively], confirming that the nonlinear multimode waveguide showed a low dispersion value. This enabled flexible positioning of the signal at wavelengths relatively far from the perfect phase matching position (≈1600 nm), without a significant CE reduction.

7. CONCLUSIONS

In this work, we presented the design, fabrication and characterization of a fully integrated, IM-FWM-based wavelength converter realized on a Si-rich SiN platform. The wavelength converter was designed to operate using a dual-pump BS-IM-FWM configuration that employed the first two horizontal spatial modes (TE_{00} and TE_{10}) of a multimode waveguide. The choice of the Si-rich SiN material provided an additional degree of freedom in the waveguide design compared to standard platforms thanks to the possibility of carefully controlling the refractive index of the deposited layers. In addition, it allowed us to perform nonlinear experiments with relatively high CW pump power levels (>27 dBm), with no sign of detrimental TPA- and free carrier absorption (FCA)-related losses [37,38]. The whole set of mode conversion, multiplexing and demultiplexing functionalities was performed on-chip, with the input/output signals coupled in/out from the chip using two arrays of two lensed single-mode PM optical fibers each. This significantly simplified the experimental setup compared to previous demonstrations of intermodal nonlinearities [12,20,21], reduced the insertion losses of the whole system and removed the requirement to filter out the optical pumps at the output of the device. The system was designed to convert a seeding L-band signal to longer wavelengths by employing optical pumps located in the C- and L-bands. A 3 dB bandwidth for the conversion process exceeding 70 nm was demonstrated, showing the possibility of generating idler components covering the whole U-band. This represents, to the best of the authors' knowledge, the widest bandwidth ever demonstrated for an IM-FWM-based device. The maximum value of the CE was measured to be equal to ≈ − 41 dB, mainly limited by the current Si-rich SiN material losses and the relatively short length (1 cm) of the nonlinear multimode waveguide employed in our particular implementation. Comparable CE values were reported in IM-FWM-based wavelength converters implemented in multimode silicon waveguides using CW optical pumps [21–23]. Further improvements in the material quality and fabrication process will result in a significant reduction of the propagation losses of our material, thus enabling the utilization of longer nonlinear multimode waveguides and thereby achieving higher CE values. In this regard, we previously reported CE values as high as −15 dB using a BS-IM-FWM scheme in a Si-rich SiN platform with a different material composition (refractive index of 2.54 at 1550 nm) thanks to the use of a 4 cm long nonlinear multimode waveguide (propagation losses equal to 0.95 dB/cm at 1550 nm), with off-chip optical mode manipulation [20]. Additionally, the implementation of longer low-loss nonlinear waveguide sections would allow the use of lower pump power levels compared to the relatively high ones used in this work (27.6 dBm total pump power). One attractive route for the material optimization is represented by the use of high-temperature (>1000°C) thermal annealing processes, which have been widely exploited to significantly decrease the losses of stoichiometric silicon nitride (Si_3N_4, refractive index of ≈2 at 1550 nm), resulting in waveguide propagation losses lower than 0.05 dB/cm [38,48]. These techniques have already proven to be effective even for Si-rich SiN platforms slightly enriched in the silicon content (refractive index of 2.07 at 1550 nm) compared to Si_3N_4, with measured propagation losses as low as 0.4 dB/cm [49]. In conclusion, the demonstrated device shows the potential of the BS-IM-FWM phase matching scheme and marks a noteworthy advancement towards the realization of a fully integrated, highly tunable frequency synthesizer capable of operating within optical bands with hundreds of nanometers separation. It is worth noting that, when compared to other IM nonlinear processes, the BS-IM-FWM configuration has the potential to convert photons from the signal to the newly generated idler frequencies without excess noise, entailing far-reaching implications for both classical telecommunications and quantum systems. Appropriate adaptation of the design of the integrated mode-MUX and -DEMUX devices would allow the nonlinear multimode waveguide to operate with higher-order spatial modes, potentially leading to the realization of compact and tunable MIR sources. These developments could hold profound implications across a diverse spectrum of technological applications, encompassing gas sensing [50], molecular spectroscopy [51], medicine and biology [52], free space telecommunication [53] and quantum optics [54].

APPENDIX A: INTEGRATED DEVICE DIMENSIONS

Figure 10 shows a schematic view of the left side of the designed integrated system with the parameter names used to indicate the device dimensions. The right side of the device, not shown in the figure, is a mirrored copy of the left side and has the same

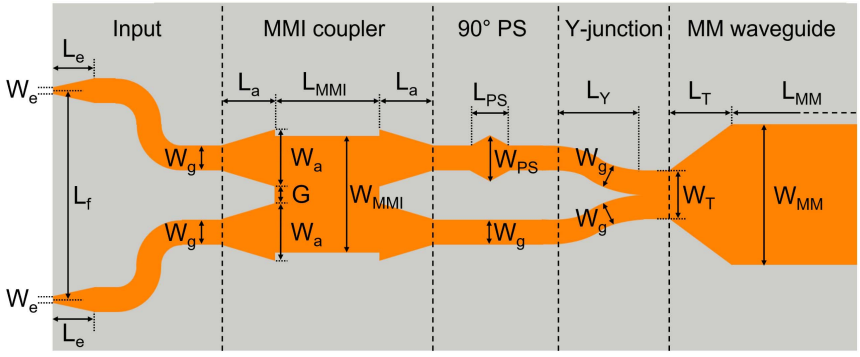

Fig. 10. Schematic view of the left side of the integrated wavelength converter with the parameter names used to indicate the device dimensions. MMI coupler, multimode interference coupler; PS, phase shifter; MM waveguide, multimode waveguide.

Table 1. Device Geometrical Parameters[a]

Component	Parameter		Value
SM waveguide	Width	W_g	0.5 μm
Input section	Edge coupler tip	W_e	0.228 μm
	Edge coupler length	L_e	125 μm
	Input separation	L_f	250 μm
MMI coupler	Taper length	L_a	18.5 μm
	Access width	W_a	1.5 μm
	Gap	G	1 μm
	MMI length	L_{MMI}	39.8 μm
	MMI width	W_{MMI}	3.85 μm
90° phase shifter	PS width	W_{PS}	0.69 μm
	PS length	L_{PS}	5.2 μm
Y-junction	Stem width	W_T	1 μm
	Arm length	L_Y	28.64 μm
MM waveguide	Taper length	L_T	200 μm
	Waveguide length	L_{MM}	1 cm
	Waveguide width	W_{MM}	6.1 μm

[a]SM waveguide, single-mode waveguide; MMI coupler, multimode interference coupler; PS, phase shifter; MM waveguide, multimode waveguide.

dimensions. Table 1 reports the full list of the device geometrical parameters and their respective values.

Funding. Engineering and Physical Sciences Research Council (EP/R003076/1, EP/T007303/1, EP/W024772/1); Ministero dell'Università e della Ricerca (PRIN (2022H7RR4F)).

Acknowledgment. The use of the IRIDIS High Performance Computing Facility at the University of Southampton is acknowledged. The fabrication was carried out at the Southampton Nanofabrication Centre, part of the Zepler Institute, at the University of Southampton, United Kingdom.

Disclosures. The authors declare no conflicts of interest.

Data Availability. Data underlying the results presented in this paper are available from the corresponding author upon reasonable request.

REFERENCES

1. D. Dai and J. E. Bowers, "Silicon-based on-chip multiplexing technologies and devices for peta-bit optical interconnects," Nanophotonics **3**, 283–311 (2014).
2. I. Cristiani, C. Lacava, G. Rademacher, *et al.*, "Roadmap on multimode photonics," J. Opt. **24**, 083001 (2022).
3. Y. Su, Y. He, H. Chen, *et al.*, "Perspective on mode-division multiplexing," Appl. Phys. Lett. **118**, 200502 (2021).
4. S. Berdagué and P. Facq, "Mode division multiplexing in optical fibers," Appl. Opt. **21**, 1950–1955 (1982).
5. J. Renaudier, A. Napoli, M. Ionescu, *et al.*, "Devices and fibers for ultrawideband optical communications," Proc. IEEE **110**, 1742–1759 (2022).
6. A. Ferrari, A. Napoli, J. K. Fischer, *et al.*, "Assessment on the achievable throughput of multi-band ITU-T G.652.D fiber transmission systems," J. Lightwave Technol. **38**, 4279–4291 (2020).
7. J. Leuthold, C. Koos, and W. Freude, "Nonlinear silicon photonics," Nat. Photonics **4**, 535–544 (2010).
8. M. A. Foster, A. C. Turner, J. E. Sharping, *et al.*, "Broad-band optical parametric gain on a silicon photonic chip," Nature **441**, 960–963 (2006).
9. S. Zlatanovic, J. S. Park, S. Moro, *et al.*, "Mid-infrared wavelength conversion in silicon waveguides using ultracompact telecom-band-derived pump source," Nat. Photonics **4**, 561–564 (2010).
10. A. Ayan, F. Mazeas, J. Liu, *et al.*, "Polarization selective ultra-broadband wavelength conversion in silicon nitride waveguides," Opt. Express **30**, 4342–4350 (2022).
11. Y. Franz, J. Haines, C. Lacava, *et al.*, "Strategies for wideband light generation in nonlinear multimode integrated waveguides," Phys. Rev. A **103**, 013511 (2021).
12. S. Signorini, M. Mancinelli, M. Borghi, *et al.*, "Intermodal four-wave mixing in silicon waveguides," Photon. Res. **6**, 805–814 (2018).
13. R. Kou, A. Ishizawa, K. Yoshida, *et al.*, "Spatially resolved multimode excitation for smooth supercontinuum generation in a SiN waveguide," Opt. Express **31**, 6088–6098 (2023).
14. A. ben Khalifa, A. B. Salem, and R. Cherif, "Multimode supercontinuum generation in As_2S_3 chalcogenide photonic crystal fiber," in *Frontiers in Optics* (Optica, 2018), paper JTu2A-18.
15. R. Dupiol, K. Krupa, A. Tonello, *et al.*, "Interplay of Kerr and Raman beam cleaning with a multimode microstructure fiber," Opt. Lett. **43**, 587–590 (2018).
16. Y. Zhang, K. Zhong, G. Hu, *et al.*, "Sub-milliwatt optical frequency combs in dual-pumped high-Q multimode silicon resonators," Appl. Phys. Lett. **117**, 221103 (2020).
17. Y. Zhang, G. Hu, K. Zhong, *et al.*, "Investigation of low-power comb generation in silicon microresonators from dual pumps," J. Opt. **23**, 10LT03 (2021).
18. Y. Liu, A. Choudhary, G. Ren, *et al.*, "Circulator-free Brillouin photonic planar circuit," Laser Photon. Rev. **15**, 2000481 (2021).
19. E. A. Kittlaus, N. T. Otterstrom, and P. T. Rakich, "On-chip inter-modal Brillouin scattering," Nat. Commun. **8**, 15819 (2017).
20. C. Lacava, T. D. Bucio, A. Khokhar, *et al.*, "Intermodal frequency generation in silicon-rich silicon nitride waveguides," Photon. Res. **7**, 615–621 (2019).
21. C. Lacava, M. A. Ettabib, T. D. Bucio, *et al.*, "Intermodal Bragg-scattering four wave mixing in silicon waveguides," J. Lightwave Technol. **37**, 1680–1685 (2019).
22. S. Signorini, M. Finazzer, M. Bernard, *et al.*, "Silicon photonics chip for inter-modal four wave mixing on a broad wavelength range," Front. Phys. **7**, 128 (2019).
23. G. Ronniger, I. Sackey, T. Kernetzky, *et al.*, "Efficient ultra-broadband C-to-O band converter based on multi-mode silicon-on-insulator waveguides," in *European Conference on Optical Communication (ECOC)* (IEEE, 2021), pp. 1–4.
24. S. Liang, Y. Jung, K. R. Bottrill, *et al.*, "L-band mode and wavelength conversion in a periodically poled lithium niobate ridge waveguide," in *European Conference and Exhibition on Optical Communication* (Optica, 2022), paper Tu5-22.
25. S. Signorini, M. Sanna, S. Piccione, *et al.*, "A silicon source of heralded single photons at 2 μm," APL Photon. **6**, 126103 (2021).
26. L.-T. Feng, M. Zhang, X. Xiong, *et al.*, "On-chip transverse-mode entangled photon pair source," npj Quantum Inf. **5**, 2 (2019).
27. S. Paesani, M. Borghi, S. Signorini, *et al.*, "Near-ideal spontaneous photon sources in silicon quantum photonics," Nat. Commun. **11**, 2505 (2020).
28. C. J. McKinstrie, S. Radic, and M. Raymer, "Quantum noise properties of parametric amplifiers driven by two pump waves," Opt. Express **12**, 5037–5066 (2004).
29. C. McKinstrie, M. Yu, M. Raymer, *et al.*, "Quantum noise properties of parametric processes," Opt. Express **13**, 4986–5012 (2005).
30. C. McKinstrie, J. Harvey, S. Radic, *et al.*, "Translation of quantum states by four-wave mixing in fibers," Opt. Express **13**, 9131–9142 (2005).
31. Q. Li, M. Davanço, and K. Srinivasan, "Efficient and low-noise single-photon-level frequency conversion interfaces using silicon nanophotonics," Nat. Photonics **10**, 406–414 (2016).
32. I. Agha, S. Ates, M. Davanço, *et al.*, "A chip-scale, telecommunications-band frequency conversion interface for quantum emitters," Opt. Express **21**, 21628–21638 (2013).

33. A. C. Turner, C. Manolatou, B. S. Schmidt, *et al.*, "Tailored anomalous group-velocity dispersion in silicon channel waveguides," Opt. Express **14**, 4357–4362 (2006).
34. K. Li, H. Sun, and A. C. Foster, "Four-wave mixing Bragg scattering in hydrogenated amorphous silicon waveguides," Opt. Lett. **42**, 1488–1491 (2017).
35. F. Parmigiani, P. Horak, Y. Jung, *et al.*, "All-optical mode and wavelength converter based on parametric processes in a three-mode fiber," Opt. Express **25**, 33602–33609 (2017).
36. S. M. M. Friis, I. Begleris, Y. Jung, *et al.*, "Inter-modal four-wave mixing study in a two-mode fiber," Opt. Express **24**, 30338–30349 (2016).
37. C. Lacava, S. Stankovic, A. Z. Khokhar, *et al.*, "Si-rich silicon nitride for nonlinear signal processing applications," Sci. Rep. **7**, 22 (2017).
38. F. Gardes, A. Shooa, G. De Paoli, *et al.*, "A review of capabilities and scope for hybrid integration offered by silicon-nitride-based photonic integrated circuits," Sensors **22**, 4227 (2022).
39. E. D. Palik, *Handbook of Optical Constants of Solids* (Academic, 1998), Vol. **3**.
40. P. Horak and F. Poletti, "Multimode nonlinear fibre optics: theory and applications," in *Recent Progress in Optical Fiber Research* (IntechOpen, 2012), Vol. **3**.
41. D. González-Andrade, J. G. Wangüemert-Pérez, A. V. Velasco, *et al.*, "Ultra-broadband mode converter and multiplexer based on subwavelength structures," IEEE Photon. J. **10**, 2201010 (2018).
42. D. González-Andrade, A. Dias, J. G. Wangüemert-Pérez, *et al.*, "Experimental demonstration of a broadband mode converter and multiplexer based on subwavelength grating waveguides," Opt. Laser Technol. **129**, 106297 (2020).
43. T. D. Bucio, A. Z. Khokhar, C. Lacava, *et al.*, "Material and optical properties of low-temperature NH_3-free PECVD SiN_x layers for photonic applications," J. Phys. D **50**, 025106 (2016).
44. L. Carpenter, S. Berry, and C. Gawith, "Ductile dicing of $LiNbO_3$ ridge waveguide facets to achieve 0.29 nm surface roughness in single process step," Electron. Lett. **53**, 1672–1674 (2017).
45. P. C. Gow, G. M. Churchill, V. Vitali, *et al.*, "Ductile dicing for optical facets and waveguides in silicon nitride," in *Conference on Lasers and Electro-Optics Europe & European Quantum Electronics Conference (CLEO/Europe-EQEC)* (IEEE, 2023), p. 1.
46. D. González-Andrade, R. F. de Cabo, J. Vilas, *et al.*, "Mode converter and multiplexer with a subwavelength phase shifter for extended broadband operation," IEEE Photon. Technol. Lett. **33**, 1262–1265 (2021).
47. D. González-Andrade, J. M. Luque-González, J. G. Wangüemert-Pérez, *et al.*, "Ultra-broadband nanophotonic phase shifter based on subwavelength metamaterial waveguides," Photon. Res. **8**, 359–367 (2020).
48. Z. Ye, P. Zhao, K. Twayana, *et al.*, "Overcoming the quantum limit of optical amplification in monolithic waveguides," Sci. Adv. **7**, eabi8150 (2021).
49. Z. Ye, A. Fülöp, Ó. B. Helgason, *et al.*, "Low-loss high-*Q* silicon-rich silicon nitride microresonators for Kerr nonlinear optics," Opt. Lett. **44**, 3326–3329 (2019).
50. D. Popa and F. Udrea, "Towards integrated mid-infrared gas sensors," Sensors **19**, 2076 (2019).
51. M. Vainio and L. Halonen, "Mid-infrared optical parametric oscillators and frequency combs for molecular spectroscopy," Phys. Chem. Chem. Phys. **18**, 4266–4294 (2016).
52. K. Isensee, N. Kröger-Lui, and W. Petrich, "Biomedical applications of mid-infrared quantum cascade lasers–a review," Analyst **143**, 5888–5911 (2018).
53. Y. Su, W. Wang, X. Hu, *et al.*, "10 Gbps DPSK transmission over free-space link in the mid-infrared," Opt. Express **26**, 34515–34528 (2018).
54. L. M. Rosenfeld, D. A. Sulway, G. F. Sinclair, *et al.*, "Mid-infrared quantum optics in silicon," Opt. Express **28**, 37092–37102 (2020).